



Flexible and high precision thermal metasurface

Jiyao Wang ^{1,2}, Ling Qin^{1,2} & Wei Xu ¹✉

Thermal metamaterials are artificial materials used to manipulate heat flow in many applications, such as thermal protection, thermal camouflage, and precise temperature control. Most of the existing thermal metamaterials are mainly based on metal, which makes their fabrication complex and time-consuming, and limits their flexibility. Here, we show a strategy to simplify the fabrication process, improve machining accuracy, and realize flexibility in thermal metasurfaces. Our proposed thermal metasurface is fabricated by laser engraving of copper-graphene coating surface, utilizing graphene coating with high thermal conductivity instead of the traditional filling materials of low thermal conductivity. It maintains the integrity of copper substrate, giving the metasurface a good heat dispersion. Controlled temperature gradient patterns are established, and the metasurface can be bent without changing its features, except for a slight variation in its thermal gradient. Finally, its cloaking ability is demonstrated by camouflaging the same heat source in the shape of different objects. Our designed metasurface mitigates the limitations in design and fabrication of existing thermal metamaterials, and can be used in applications requiring large flexibility, thermal illusion, and large thermal gradients on small scales.

¹School of Electrical Engineering, Southeast University, Nanjing, Jiangsu Province, China. ²These authors contributed equally: Jiyao Wang, Ling Qin.
✉email: weixu@seu.edu.cn

Thermal energy that is one of the most common energy sources in the world, is an important part of human daily life and social production^{1,2}. The heat transfer, which has three modes: heat conduction, heat convection, and heat radiation, is a complex diffusion process leading to difficulties in utilization and manipulation. Metamaterials that are an artificial arrangement of the traditional materials, can achieve functions that traditional materials cannot realize³, which provide additional capability to manipulate heat flow. The advent of transformation optics and controlling electromagnetic fields provide a systematic method for the metamaterials design^{4,5} and are extended to transformation thermotics.

Based on the theory of transformation optics, the steady-state theory of transformation thermotic is proposed and developed to obtain the cloaking and concentration of heat flow^{6–15}. It has great potential in many applications, such as thermal protection, thermal camouflage, and precise temperature control. Further, the nonsteady-state theory of transformation thermotic is proposed. The thermal cloaking and concentration by multilayered homogeneous isotropic materials are achieved to replace anisotropic materials, which supplies the possibility for the actual preparation of thermal metamaterials¹⁶. Utilizing the multilayer composite approach, several artificial metamaterials are designed, fabricated, and characterized to realize the shield, concentration, and inversion of heat flow^{17–24}. Meanwhile, a way of controlling heat transportation is developed by introducing the concept of “thermocystals.” It has periodic structures made of alloys containing nanoparticles and inspired many thermal effects and devices²⁵. These characteristics, such as shield, concentration, and inversion of heat flow, of the artificial thermal metamaterials, are significantly different from those of traditional materials and thus attract more and more research interests^{26–28}. Since then, thermal metamaterials have developed rapidly.

The three-dimensional (3D) thermal cloak metamaterial is proposed to decrease the influence of external heat flux on the inner air bubbles. It was designed and fabricated by the 3D metal processing technology, upgrading the previous thermal metamaterials from 2D to 3D and expanding the application prospects²⁹. Bilayer thermal cloak that is composed of the inner and outer layer with different materials is proposed to simplify the design and manufacturing of the thermal cloak³⁰. Meanwhile, the same author proposes the thermal camouflage metamaterial device to alter the thermal appearance signature of an object to that of multiple isolated expected targets³¹. Thermal camouflage device has a very high value in military applications, and set off an upsurge in the research of heat camouflage technology^{32–44}. The macroscopic thermal diode is theoretically proposed⁴⁵. Bimetallic or memory alloys structures are utilized to obtain nonlinear functions according to the structural transformation of the components in different direction through the heat flux, which has several potential applications, such as heat preservation, heat dissipation, and energy saving^{46,47}. The development of thermal metamaterials supplied a strategy for the protection of electronic devices and increased power density in microelectronic packaging. However, the existing major metamaterials are large-scale, and it is difficult to apply them to the highly integrated electronic packaging. Thus, a potential strategy in the anisotropic thermal conductivity of multilayer printed circuit boards (PCBs) for on-board heat flow control is designed and experimental verified, which can be considered as an additional way improving highly integrated electronics^{48,49}. For simplifying the manufacturing process, a tuneable thermal metamaterial using the assembly of unit-cell thermal shifters is designed and experimentally verified for electronic device protection^{50,51}. It is worth mentioning that the minimum linewidth of the copper in the unit cell is 250 μm .

The thermal metamaterials mentioned above are essentially materials with different thermal conductivity arranged in a specific structure to achieve different functions. It is a crucial issue that how to design the optimal structure for specific target applications. For this, the computational optimization method is applied for the coaching design of heat cloak, heat concentrator, and heat reversal⁵². With the rapid development of interdisciplinary science, different topology optimization methods, such as particle swarm optimization-based algorithms, CMA-ES (covariance matrix adaptation evolution strategy), machine-learning, and effective medium, are used in guiding and designing thermal metamaterials in single and multiple physical fields. These optimization methods provide a systematic guideline for the metamaterial design and thus improve design efficiency^{48,52–65}. However, the optimized structure is usually complex and mainly metal based, which requires precise manufacturing equipment (for example, computerized numerical control (CNC) machine). It is complicated and time-consuming from a fabrication perspective and does not have flexibility.

Herein, we propose and demonstrate a flexible-high precision thermal metasurface based on copper-graphene material in order to further simplify the fabrication process, improve thermal manipulation precision in small scale, reduce costs, and achieve overall flexibility. The proposed thermal metasurface utilizes graphene coating instead of the traditional filling materials of low thermal conductivity and it maintains the integrity of the copper substrate. Thus, the thermal conductive of the whole thermal metasurface device can be improved, which is conducive to target system heat dissipation. Meanwhile, the graphene coating has durable, noncracking, and anticorrosive^{66–71} which makes the thermal metasurface work even in harsh environment.

Results

High-resolution thermal surface. To start, a copper foil is utilized as the base material providing flexibility. Subsequently, the graphene water solution is coated on the surface of copper foil. After leaving it in the air for an hour, the copper-graphene coating (CGC) material is established (see Fig. 1a). The thickness of copper foil and CGC material are 30 and 70 μm , which are measured by vernier micrometer (see Supplementary Fig. 2), respectively. The copper and graphene coating are in close contact, which reduces the thermal contact resistance between the two materials. The graphene coating also acts as a protective film covering the surface of the experimental materials, protecting the metal surface from air oxidation. Thanks to the black graphene coating, the reflections to the infrared (IR, UTI85) camera, and laser are maximally decreased, which ensures both the IR thermal measurement and laser engraving accuracy.

To investigate the fabrication accuracy, we select the logos of “COMMUN. MATER.” (CM) (see Fig. 1b(i)) and “SOUTHEAST UNIVERSITY” (SEU) (see Fig. 1c(i)) as the processing targets using carbon dioxide (CO_2) laser engraving machine, respectively. The laser-machined surfaces are shown in Fig. 1b(ii) and 1c(ii). In this paper, we refer them as “CM logo surface” and “SEU logo surface” for conveniently describing. The dimension and topology of CM and SEU logo surface are shown in Supplementary Fig. 2. The length of CM logo surface is 41.92 mm and the diameter of SEU logo surface is 30.38 mm.

As shown in Fig. 1b(iii), we zoomed the character “N” through an electronic magnifier to explore sculptural details and measure the linewidth of the character. It can be seen that the thickness of the carved area is lower than that of the uncarved area (see Supplementary Fig. 2). Thus, the thermal resistance of the uncarved area (R_{punc}) is higher than that of the carved area (R_{pc}) in the direction perpendicular to the CM logo surface. If the CM logo



Fig. 1 The processes of the CGC materials, CM logo, and SEU logo surfaces. **a** The schematic of CGC materials. **b** (i) Selection a CM logo; (ii) Engraving the CGC material through CO₂ laser engraving machine to form the CM logo surface; (iii) Zooming in the red dashed box of CM logo surface to observe the detail of the processing and measure the linewidth through the electronic magnifying glass; The linewidth of char “N” is 1.80 mm; (iv and iv reference) Taking photos using an IR camera with and without heat source. **c** (i) Selection a complex logo; (ii) Engraving the CGC material through CO₂ laser engraving machine to form the SEU logo surface; (iii) (iii) Zooming in the red dashed box of the SEU logo surface to observe the smoothness of the curve and measure the linewidth; The linewidth of the curve and bold straight line are the 0.47 and 0.86 mm; (iv and iv reference) Taking photos of the SEU using an IR camera with and without attaching to the surface of heat source.

surface is attached to the heat panel, the carved area and the uncarved area will form a temperature difference due to the different thermal resistances. The two areas thus display different colors leading to revealing the carved information under the IR camera. For verification, the IR thermal image of the CM logo surface is taken without heat source (see Fig. 1b(iv reference)). The CM logo surface cannot be recognized. As a comparison, we then attach the CM logo surface onto a heat panel and take another thermal image with an IR camera. The thermal image shown in Fig. 1b(iv) clearly displays the information of the CM logo surface and thus demonstrates the high thermal resolution. Even though the linewidth of letter “N” is 1.80 mm (see Fig. 1b(iii)), the IR camera can still capture the precise shape of the character.

To further investigate the thermal resolution of the proposed fabrication method on complex shapes with narrow linewidth, the SEU logo containing points, arcs, straight lines, Chinese, and English characters is selected (see Fig. 1c(i)). Such a complex logo can be finished in just a few minutes by CO₂ laser engraving

machine. We zoom the area of the red dashed box in the SEU logo surface and measure the linewidth of the curve (see Fig. 1c(ii) and 1c(iii)). The curve with a linewidth of 0.47 mm is achieved without burrs. Subsequently, the experiment without attaching the heat plate is carried out Fig. 1c(iv reference)). As shown Fig. 1c(iv reference), it shows the undecipherable experiment result which is the same with that of the CM logo surface. The IR thermal image of the SEU logo surface is also taken by attaching to the heat panel (see Fig. 1c(iv)). Even though the logo is complex, the thermal resolution of the SEU logo surface is clearly demonstrated in Fig. 1c(iv). The curve with the linewidth of 0.47 mm can be clearly identified and even Chinese characters have a certain degree of recognition, which demonstrates the high thermal resolution. The detailed experiment step is shown in Supplementary Fig. 3. In summary, when the thermal surface with a specific message is attached to the heat panel, we can obtain certain identifiable information through an IR camera regardless of day and night, which shows potential military application value.

Thermal metasurface. Thermal conduction is the movement of a heat flux from a high-temperature region toward a low-temperature region. To gain control over the path of heat flux transport via thermal conduction in the direction parallel to the surface of the CGC material, one needs to design an artificial material with anisotropic thermal conductivity. This kind of material can be built by stacking up composite macroscopic layers of isotropic materials. According to the previous section, the metasurface has high resolution under the IR camera that shows the obvious thermal conductivity difference between the carved and uncarved areas. Thus, the carved and uncarved areas form two materials with different thermal conductivity (k_c and k_{uc}), laying the foundation for manufacturing the proposed thermal metamaterials. In order to facilitate numerical analysis of thermal conduction, we make the following assumptions:

- (1) The thickness of the CGC material is $70\ \mu\text{m}$ (see Supplementary Fig. 2), which is similar to that of a piece of ordinary A4 paper. Thus, in order to facilitate the analysis, we assume that the CGC material is a two-dimensional (2D) plane;
- (2) The coating after the carving is very thin and close to copper foil (see Supplementary Fig. 2). Thus, the thermal conductivity of the laser-engraved area is calculated approximately using the thermal conductivity of copper ($400\ \text{W m}^{-1}\ \text{K}^{-1}$)⁷².

The 2D diffusion thermal conduction equation can be written as:

$$\rho C \frac{\partial T}{\partial t} + \nabla(-k\nabla T) = S \quad (1)$$

where ρ is the density (kg m^{-3} , i.e., kilogram per cubic meter in SI units), C is the specific heat capacity ($\text{J kg}^{-1}\ \text{K}^{-1}$, i.e., joule per kilogram Kelvin in SI units), T is the temperature (K), k is the thermal conductivity ($\text{W m}^{-1}\ \text{K}^{-1}$, i.e., watt per meter kelvin in SI units), and S is a heat source. Based on the thermal conduction equation (Eq. (1)), we design and analyze a $6 \times 6\ \text{mm}$ thermal unit block (TUB) metasurface utilizing the COMSOL Multiphysics finite element analysis tool. The TUB metasurface has 30 alternating layers (0.21 mm width carved area (orange in Fig. 2a) and 0.19 mm width uncarved area (gray in Fig. 2a)). Figure 2b and Fig. 2c show the temperature distribution maps and isothermal lines of uncarved CGC material (as the thermal reference) and carved TUB metasurface obtained from COMSOL Multiphysics finite element in contact with same temperature sources at both up and downsides. The simulation result for the thermal reference device reveals a temperature gradient ($\nabla T = 0.439\ \text{degC}\cdot\text{mm}^{-1}$) in the center region, as measured from point P1 to point P2 defined in Fig. 2b. An approximate 52% reduction in the temperature gradient is obtained with $\nabla T = 0.212\ \text{degC}\cdot\text{mm}^{-1}$ by using the TUB metasurface (see Fig. 2c). Meanwhile, comparing the $43.5\ \text{degC}$ isotherm line of

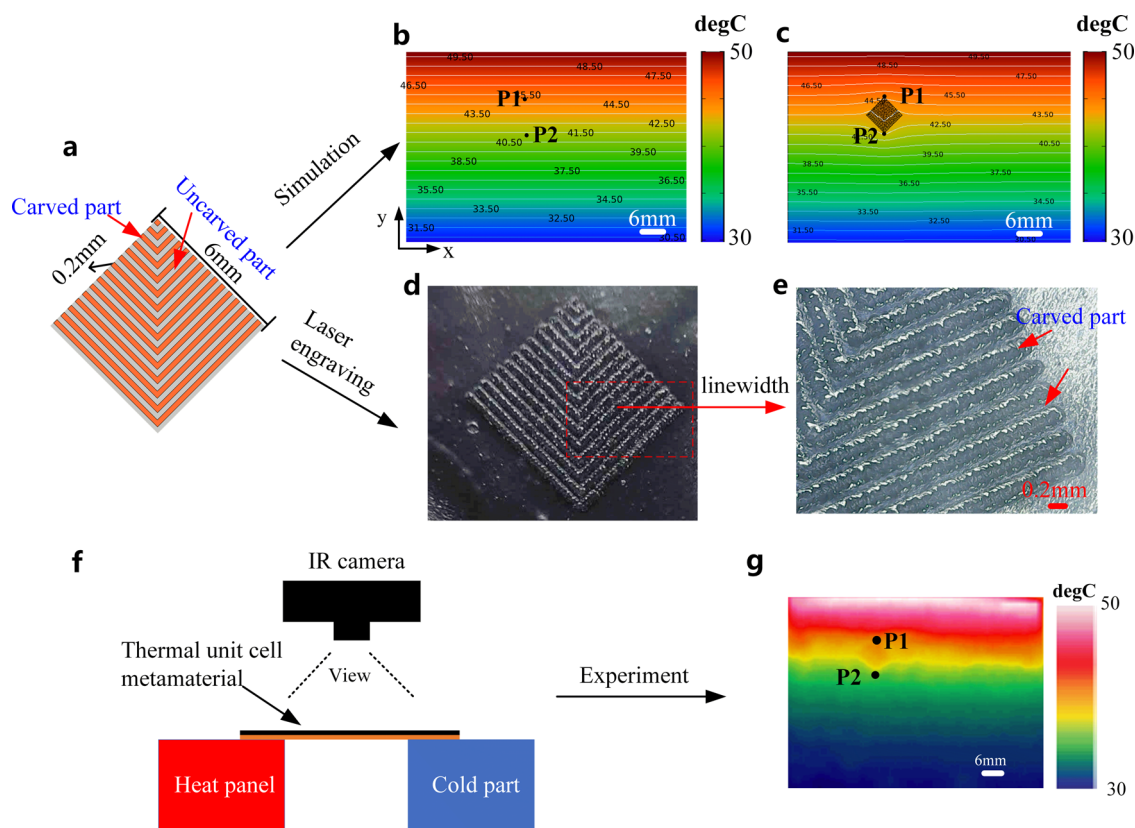


Fig. 2 Simulative and experimental performance evaluation of temperature map with thermal unit block (TUB) metasurface in contact with same temperature sources at both up and downsides. **a** Structure of the TUB metasurface. The side length of the model is 6 mm; the average linewidth of the carved area is $210\ \mu\text{m}$ and that of the uncarved area is $190\ \mu\text{m}$. **b** Temperature map without TUB metasurface obtained from numerical simulation (as the thermal reference). **c** Temperature profiles of TUB metasurface obtained from numerical simulation. **d** The TUB metasurface carved by CO_2 laser engraving processing. **e** Zooming in the red dashed box of Fig. 2d to observe the detail of the processing and measure the linewidth of the unit block through the electronic magnifying glass. **f** Scheme of the experimental apparatus illustrating the method for temperature measurement via IR camera. **g** Temperature profiles of temperature-responsive TUB metasurface obtained from experimental measurement.

Fig. 2b, c, it is observed that there is a large temperature change at the same horizontal position. The TUB metasurface is constructed by CO₂ laser engraving processing (see Fig. 2d). The partial enlarged part in the red dashed box of Fig. 2d is shown in Fig. 2e to reveal the detail of processing. Although there are some burrs, the overall linewidth distribution is relatively uniform under the electronic magnifying glass. The measured average linewidth of the carved area is about 210 μm , and the average linewidth of the uncarved area is about 190 μm that demonstrates the high processing precision. The scheme of the temperature measurement via IR camera is shown in Fig. 2f. The thermal IR camera is placed above the TUB metasurface to capture the temperature distribution. In COMSOL simulation, the TUB metasurface device is placed under hot and cold temperature boundary conditions at up and downsides. The temperature distribution reaches steady state and the thermal map of the TUB metasurface is obtained (see Fig. 2g). The experimental result for the TUB metasurface reveals a temperature gradient ($\nabla T = 0.235 \text{ degC mm}^{-1}$) from point P1 to point P2 defined in Fig. 2g. The

temperature measurement error using the thermal IR camera was 9% compared with the simulation result due to the measurement inaccuracy and thermal radiation losses. Although existing a certain error, we can obtain the different characteristics through TUB metasurface in such a small region (36 mm^2), which shows good thermal manipulation using the proposed TUB metasurface.

Based on the TUB metasurface, we design and construct three different combinations that are the homocentric squares mode (Model I, see Fig. 3a(i)), 45-degree rotation of Model I (Model II, Fig. 3b(i)), and the combination mode of the Models I and II (Model III, Fig. 3c(i)) to obtain the different temperature distributions on the surface of CGC material. The thermal gradient for the uncarved the CGC material surface is $0.449 \text{ degC mm}^{-1}$. The simulation results for Models I and II metasurface reveal the temperature gradients ($\nabla T_{\text{SI}} = 0.164 \text{ degC mm}^{-1}$ and $\nabla T_{\text{SII}} = 0.159 \text{ degC mm}^{-1}$) measured from point P1 to point P2 defined in Fig. 3a(ii) and Fig. 3b(ii), which have approximate 63.6 and 64.7% reductions compared with that of the uncarved CGC material surface. The experimental results are obtained via IR camera

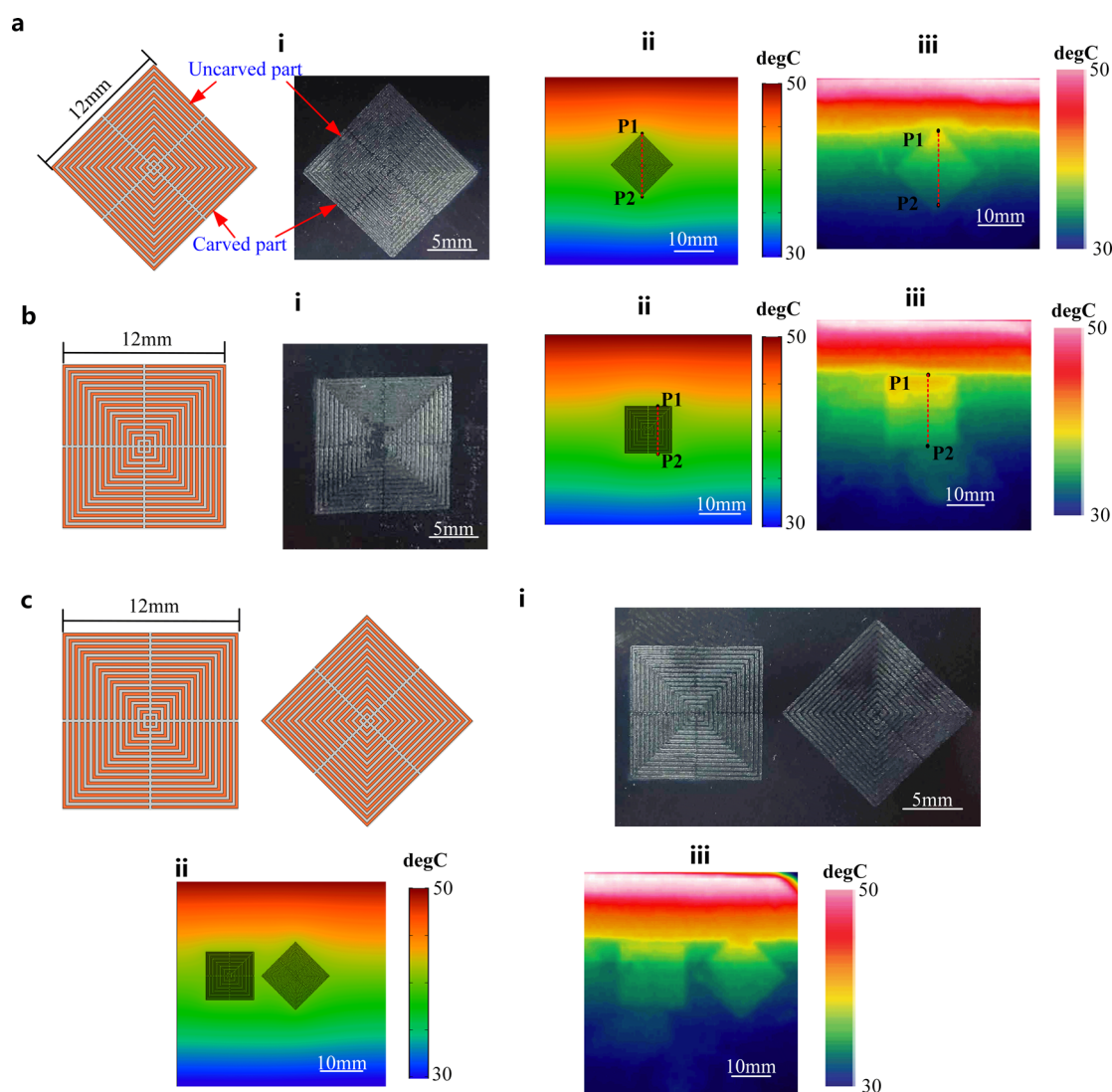


Fig. 3 Simulative and experimental performance evaluation of temperature map with the three models in contact with same temperature sources at both up and downsides. **a** (i) Model I metasurface composed of four TUBs. The side length of the model is 12 mm and the linewidth of the 0.2 mm. Simulative and experimental temperature maps of Model I are obtained by COMSOL simulation and IR camera. **b** (i) Model II metasurface. It is obtained by 45-degree rotation of the Model I metasurface. (ii and iii) Simulative and experimental temperature maps of Model II are obtained by COMSOL simulation and IR camera. **c** (i) Model III metasurface. It is composed of Model I and Model II metasurfaces. (ii and iii) Simulative and experimental thermal profiles of temperature-responsive with Model III metasurface are obtained via COMSOL simulation and IR camera.

($\nabla T_{EI} = 0.1980 \text{ degC mm}^{-1}$ and $\nabla T_{EII} = 0.179 \text{ degC mm}^{-1}$) (see Fig. 3a(iii) and Fig. 3b(iii)). Model III displays very interesting temperature gradients at the same horizontal position, as shown in Fig. 3c(ii) and Fig. 3c(iii). This temperature gradient looks like a wavy line with a certain degree of recognition. And the difference between the maximum and minimum temperature is about 2 degC, which shows the different temperature maps compared with Models I and II. These characteristics demonstrate that the different temperature maps can be obtained by different combinations of TUB metasurface. Thus, the proposed concept can achieve arbitrary temperature distribution based on the specific design of the thermal metasurface on the surface of the CGC material.

To investigate the surface flexibility on thermal properties, we further conduct the thermal experiment with thermal metasurface bended (see Fig. 4). We attach a flexible adjustable graphene heat source^{72,73} to the Model III and bend the Model III into an arch shape. Model I and II cannot interfere with each other during taking thermal distribution maps due to the arched thermal metasurface. We can obtain the thermal distribution maps of the three models from different shooting angles in the same thermal metasurface. The thermal gradient in bended Models I and II are the $\nabla T_{BI} = 0.211 \text{ degC mm}^{-1}$ and $\nabla T_{BII} = 0.195 \text{ degC mm}^{-1}$. The thermal gradients of two models ($\nabla T_{BI} = 0.211 \text{ degC mm}^{-1}$ and $\nabla T_{BII} = 0.195 \text{ degC mm}^{-1}$) in Fig. 4 show the thermal gradient that are slightly different with that of two models ($\nabla T_{EI} = 0.198 \text{ degC mm}^{-1}$ and $\nabla T_{EII} = 0.179 \text{ degC mm}^{-1}$) shown in Fig. 3. Although there is slight variation in arched CGC metasurface, the function of metasurface still exists. In summary, the limitations of existing thermal materials design and fabrication are partially mitigated and thermal metamaterials can be extended to applications requiring large flexibility and great thermal gradient in small-scale design.

Thermal illusion metasurfaces. The research of thermal illusion has flourished in recently. Thermal illusion can be realized by

utilizing the manipulation of heat fluxes to shows different shapes for the same heat source via IR camera⁷⁴.

Figure 5a(i) shows the small heat source. The specific processing mode is shown in section Method. Figure 5a(ii) shows the thermal map by applying a voltage of 7.7 V to the small heat source. The high-temperature region basically coincides with the graphene domain due to the poor thermal conductivity ($0.24 \text{ W m}^{-1} \text{ K}^{-1}$) of polyimide film (PI)⁷¹. When the small heat source is attached to the uncarved CGC surface, the thermal distributions are shown in Fig. 5a (iii). This area of heat dissipation is increased because of the high thermal conductivity copper ($400 \text{ W m}^{-1} \text{ K}^{-1}$)⁷².

In order to realize the function of thermal illusion, several artificial metasurfaces are designed and fabricated to obtain different images via IR camera for the same heat source based on the conclusions of the previous sections and multilayer composite approach¹⁶ (the details are shown in Supplementary Fig. 1). These metasurfaces are Butterfly (Fig. 5b(i)), Star (Fig. 5c(i)), Man (Fig. 5d(i)) and Woman (Fig. 5e(i)) and they are all composed of curves and straight lines. The different thermal conductivities of the carved and uncarved regions create anisotropic metasurfaces to manipulate heat flux. Meanwhile, as a contrast, the isotropic thermal surfaces that have the same size of the anisotropy thermal metasurfaces are designed and fabricated to verify the effectiveness of metasurface design. These isotropic thermal illusion surfaces are Butterfly (Fig. 5b(ii)), Star (Fig. 5c(ii)), Man (Fig. 5d(ii)) and Woman (Fig. 5e(ii)) thermal surface, respective. The same small heat source is attached to the center position of every thermal anisotropic metasurface and isotropic surface. After reaching the thermal balance of the whole device, the thermal anisotropic metasurface and isotropic surface temperature distributions captured by the IR camera are shown in Fig. 5b–e, respectively. It can be clearly seen that the isotropic thermal surfaces have relatively fuzzy identification, while the anisotropic metamaterial surfaces have obvious high identification. We can clearly identify Butterfly (Fig. 5b(ii IR)), Star

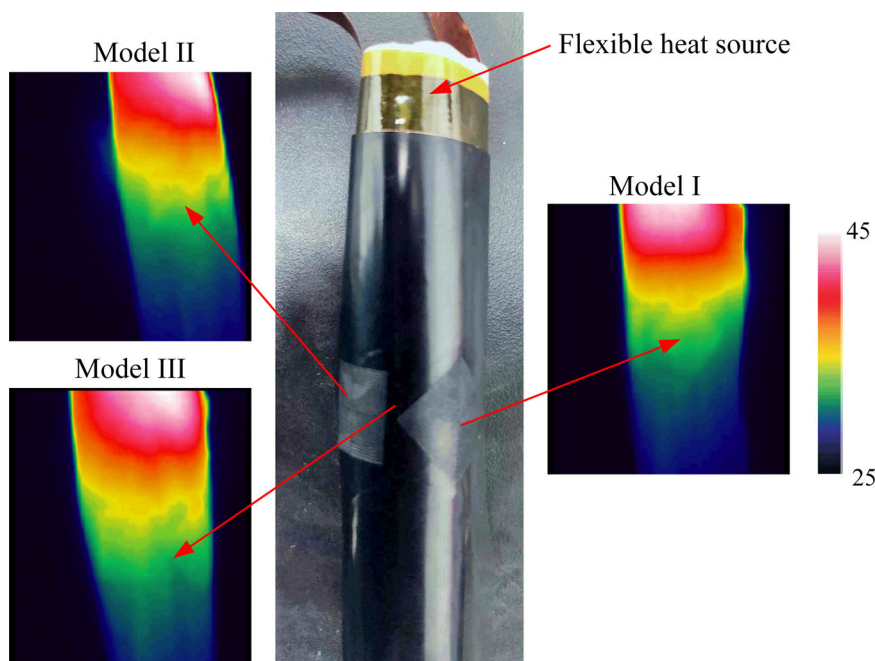


Fig. 4 Experimental performance evaluation of temperature maps to the arched thermal metasurface. A flexible adjustable graphene heat source^{72,73} is attached to the Model III and bend the Model III into an arch shape. Model I and II cannot interfere with each other during taking thermal distribution maps due to the arched thermal metasurface. The thermal distribution maps of the three models can be obtained by shooting from different angles in the same thermal metasurface.

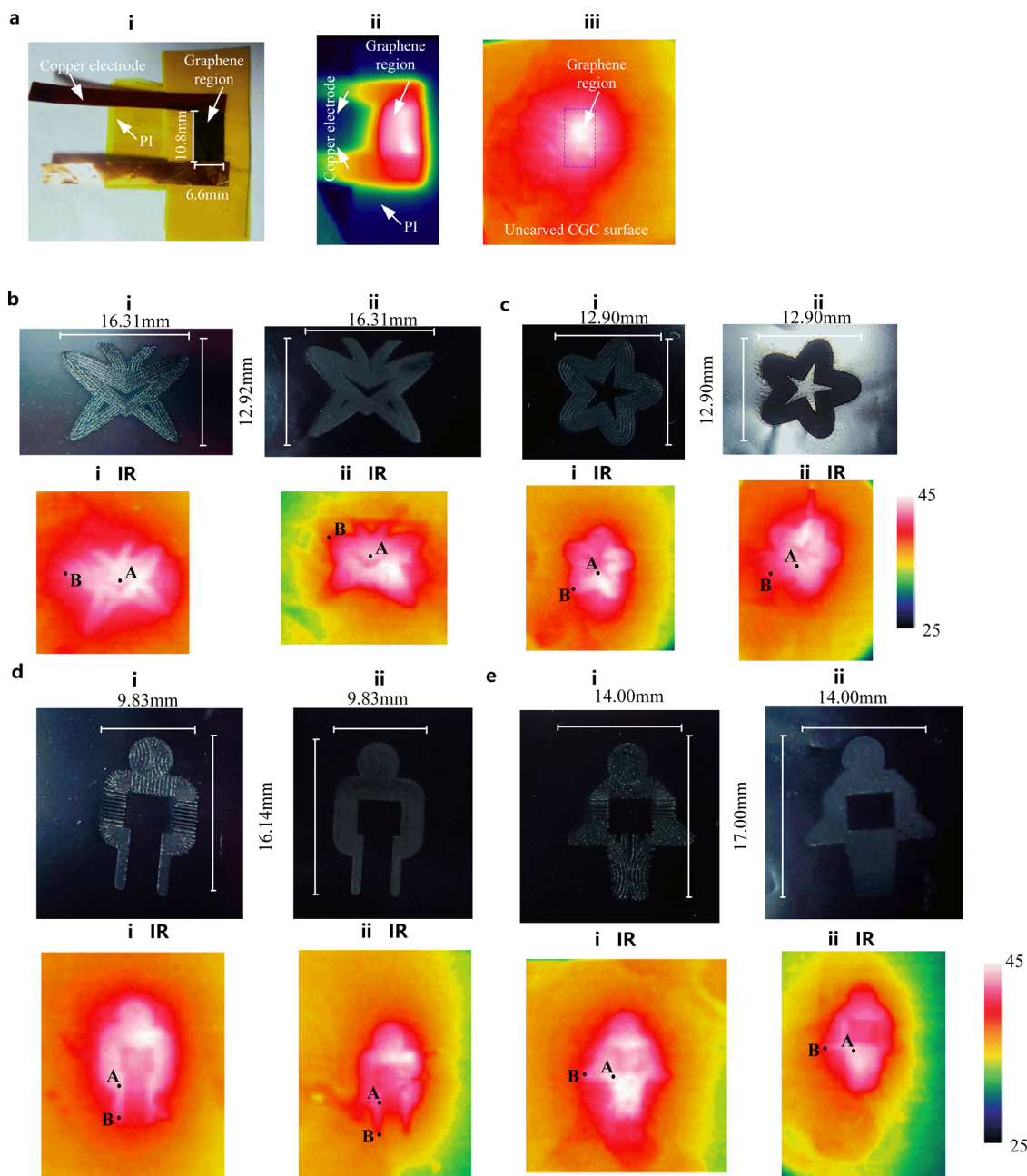


Fig. 5 Experimental performance evaluation of the anisotropic thermal illusion metasurface and isotropic thermal surface. **a** The small heat source. **b–e** The anisotropic thermal illusion metasurfaces: Butterfly(**b**(i)), Star(**c**(i)), Man(**d**(i)) and Woman(**e**(i)). The isotropic thermal illusion metasurfaces: Butterfly(**b**(ii)), Star(**c**(ii)), Man(**d**(ii)) and Woman(**e**(ii)). Attach the small heat source to them and get the thermal maps via the IR camera. The thermal maps of the Butterfly(**b**(i IR)), Star(**c**(i IR)), Man(**d**(i IR)) and Woman(**e**(i IR)) anisotropic thermal illusion metasurfaces. The thermal maps of the Butterfly(**b**(ii IR)), Star(**c**(ii IR)), Man(**d**(ii IR)) and Woman(**e**(ii IR)) isotropic thermal illusion metasurfaces.

(Fig. 5c(ii IR)), Man (Fig. 5d(ii IR)) and Woman (Fig. 5e(ii IR)) in IR photos. Thermal illusion is quantified by measuring the temperature difference between two points (A and B) in the graph. The temperature difference with different thermal shapes are shown in Table 1. The smaller the temperature difference, the thermal camouflage will be more clearly due to the small temperature difference. The radial and tangential directions thermal conductivity of the metasurfaces are different. The lower tangential thermal conductivity blocks the conduction of heat pass and reduces the heat diffusion. And the high thermal conductivity in radial direction makes the heat flux easy to conduct. Thus, the heat flux in radial directions can travel farther leading to the clearly shapes in anisotropic thermal illusion

metasurfaces than the isotropic thermal illusion surface. The proposed devices will mislead the awareness of the real shape of the actual heat sources. These results demonstrate the effectiveness of the thermal illusion metasurface design.

Discussion

We propose and experimentally validate the concept of flexible and high precision thermal metasurface. The proposed metasurface is fabricated by processing the surface of the CGC material with the CO₂ laser engraving technology. To verify the thermal gradient manipulation precision, we design and construct the CM and SEU logo surfaces. The fabrication process is simple and takes a very short

Table 1 The temperature difference between A and B in Fig. 5.

Model	Temperature difference (degC)	Model	Temperature difference (degC)
Anisotropic Man	2	Isotropic Man	4
Anisotropic Woman	3	Isotropic Woman	5
Anisotropic Star	3	Isotropic Star	4
Anisotropic Butterfly	2	Isotropic Butterfly	4

time to finish, even for the surface with SEU logo containing many complex elements. The manufacturing time of all models are shown in the Supplementary Table 2 in the supporting information. The curve with linewidth of 0.47 mm can be processed very smoothly, which demonstrates the convenience and precision of the proposed process. By attaching these two logo surfaces to the heat panel, we can clearly recognize the information on the surface via the IR camera regardless of day or night. It is worth mentioning that the curve with the linewidth of 0.47 mm in the SEU logo surface can be clearly distinguished via IR camera. These characteristics show that the proposed concept has a high thermal resolution and have military potential application value. Subsequently, we design and build the TUB metasurface (6 mm*6 mm) with the linewidth of 0.2 mm according to the difference of thermal conductivity between the carved area and the uncarved area. Two assumptions are made to simplify theoretical and simulation analysis. The first assumption is that the CGC material is a two-dimensional (2D) plane. The second assumption is the thermal conductivity of the laser-engraved area is calculated approximately using the thermal conductivity of copper ($400 \text{ W m}^{-1} \text{ K}^{-1}$). Based on thermal conduction equation, the temperature gradient distribution of the TUB metasurface in contact with hot and cold temperature sources at up and downsides is obtained by COMSOL Multiphysics finite element analysis, which shows the obvious reduction in the temperature gradient measured from point P1 to P2 compared with that of the uncarved surface of the CGC material. The experimental result is consistent with simulation result. Meanwhile, three models are designed and fabricated to obtain different thermal maps on the surface of the CGC material. Simulative and experimental results show the obvious different temperature distributions, which demonstrates that arbitrarily thermal distribution can be realized through specific metamaterial design on the surface of the CGC material. Further, the flexibility of the thermal metasurface is experimentally verified. Although existing slight variation, the functions of metasurface still exist. Based on the previous conclusions and multi-layer composite approach, four anisotropic thermal illusion metasurfaces are designed and fabricated. We successfully camouflage the shape of the rectangular heat source as a Butterfly, star, man, and woman. The device has certain function of deceiving IR camera and have certain military value. In summary, this work simplifies the conventional manufacturing process of thermal metamaterials, improves the machining accuracy, realizes the flexible and thermal illusion. Meanwhile, the performance of heat dissipation is not lost due to maintaining the integrity of the copper sheet and thus improves heat dissipation of the whole metamaterial device. Based on different requirements, different functions of thermal metasurfaces can be easily realized according to the proposed method, which expands applications of the thermal metamaterials.

Methods

Materials and devices. Electron magnifier glass was obtained from ANDONG-STAR. Graphene water-based coating was brought from Suzhou Tanfeng Graphene Technology Co. LTD. The copper foil was purchased from Taobao. The images and videos were photographed by ANDONGSTAR electron magnifier glass and Realme X2 pro. The cursor caliper was obtained from AIRAJ. The IR camera is obtained from the UNI-T and the production model is UTI85. The heat plate was obtained by Taobao and its model is LXZ-2020. CO₂ laser engraving machine was obtained from Ketai laser. The detailed parameters about the engraving machine, heat plate/source, and IR camera are shown in Supplementary Table 1. The detailed

parameters about the IR camera, heat plate, and CO₂ laser engraving machine are shown in the supporting information. ZnSe lens are obtained from Taobao.

Metasurface and heat source. The graphene is achieved by the laser-induced porous graphene films^{73,75}. The main settings of the laser engraving machine are 5.5 A current and 40 mm/s movement speed. The two pieces of copper are the positive and negative poles. All the metasurface is produced by the laser engraving (8.3 A current and 40 mm s⁻¹ speed). All thermal metasurfaces are designed by the CoreLLASER software.

Data availability

All relevant data are available from the authors upon request.

Received: 4 February 2021; Accepted: 12 August 2021;

Published online: 01 September 2021

References

- Ji, Q., Shen, X. Y. & Huang, J. P. Transformation thermotics: thermal metamaterials and their applications. *Int. J. Mod. Phys. B.* **32**, 1840004 (2018).
- Wang, J., Dai, G. L. & Huang, J. P. Thermal metamaterial: fundamental, application, and outlook. *iScience.* **23**, 101637 (2020).
- Veselago, V. G. The electrodynamics of substances with simultaneously negative values of ϵ and μ . *Physics-USPEKHI.* **10**, 509 (1968).
- Leonhardt, U. Optical conformal mapping. *Science.* **312**, 1777 (2006).
- Pendry, J. B., Schurig, D. & Smith, D. R. Controlling electromagnetic fields. *Science.* **312**, 1780 (2006).
- Fan, C. Z., Gao, Y. & Huang, J. P. Shaped graded materials with an apparent negative thermal conductivity. *Appl. Phys. Lett.* **92**, 25190767 (2008).
- Chen, T. Y., Weng, C. N. & Chen, J. S. Cloak for curvilinearly anisotropic media in conduction. *Appl. Phys. Lett.* **93**, 114103 (2008).
- Li, J. Y., Gao, Y. & Huang, J. P. A bifunctional cloak using transformation media. *J. Appl. Phys.* **108**, 074504 (2010).
- Yu, G. X., Lin, Y. F. & Zhang, G. Q. Design of square-shaped heat flux cloaks and concentrators using method of coordinate transformation. *Front. Phys.* **6**, 70 (2011).
- Peralta, I., Fachinotti, V. D. & Álvarez Hostos, J. C. A brief review on thermal metamaterials for cloaking and heat flux manipulation. *Adv. Eng. Mater.* **22**, 1901034 (2020).
- Guenneau, S., Petiteau, D., Zerrad, M., Amra, C. & Puvirajesinghe, T. Transformed Fourier and Fick equations for the control of heat and mass diffusion. *AIP Adv.* **5**, 053404 (2015).
- Han, T. C. & Qiu, C. W. Transformation Laplacian metamaterials: recent advances in manipulating thermal and dc fields. *J. Opt.* **18**, 044003 (2016).
- Kadic, M., Bückmann, T., Schittny, R. & Wegene, M. Metamaterials beyond electromagnetism. *Rep. Prog. Phys.* **76**, 126501 (2013).
- Zhang, Y. M., Xu, H. Y. & Zhang, B. L. Design, implementation, and extension of thermal invisibility cloaks. *AIP Adv.* **5**, 053402 (2015).
- Hu, R. et al. Binary thermal encoding by energy shielding and harvesting units. *Phys. Rev. Applied* **10**, 054032 (2018).
- Guenneau, S., Amra, C. & Veynante, D. Transformation thermodynamics: cloaking and concentrating heat flux. *Opt. Express* **20**, 8207 (2012).
- Narayana, S. & Sato, Y. Heat flux manipulation with engineered thermal materials. *Phys. Rev. Lett.* **108**, 214303 (2012).
- Han, T. C., Yuan, T., Li, B. W. & Qiu, C. W. Homogeneous thermal cloak with constant conductivity and tunable heat localization. *Sci. Rep.* **3**, 1593 (2013).
- Han, T. C. et al. Theoretical realization of an ultra-efficient thermalenergy harvesting cell made of natural materials. *Energy Environ. Sci.* **6**, 3537 (2013).
- Narayana, S., Savo, S. & Sato, Y. Transient heat flux shielding using thermal metamaterials. *Appl. Phys. Lett.* **102**, 201904 (2013).
- Guenneau, S. & Amra, C. Anisotropic conductivity rotates heat fluxes in transient regimes. *Opt. Express.* **21**, 6578 (2013).
- Schittny, R., Kadic, M., Guenneau, S. & Wegener, M. Experiments on transformation thermodynamics: molding the flow of heat. *Phys. Rev. Lett.* **110**, 195901 (2013).

23. Ma, Y. G., Lan, L., Jiang, W., Sun, F. & He, S. L. A transient thermal cloak experimentally realized through a rescaled diffusion equation with anisotropic thermal diffusivity. *Npg. Asia Mater.* **5**, e73 (2013).
24. Gao, Y. & Huang, J. P. Unconventional thermal cloak hiding an object outside the cloak. *Eur. Phys. Lett.* **104**, 44001 (2013).
25. Maldovan, M. Narrow low-frequency spectrum and heat management by thermocrystals. *Phys. Rev. Lett.* **110**, 025902 (2013).
26. Leonhardt, U. Cloaking of heat. *Nature*. **498**, 440 (2013).
27. Wegener, M. Metamaterials beyond optics. *Science*. **342**, 939 (2013).
28. Maldovan, M. Sound and heat revolutions in phononics. *Nature*. **503**, 209 (2013).
29. Xu, H. Y., Shi, X. H., Gao, F., Sun, H. D. & Zhang, B. L. Ultrathin three-dimensional thermal cloak. *Phys. Rev. Lett.* **112**, 054301 (2014).
30. Han, T. C. et al. Experimental demonstration of a bilayer thermal cloak. *Phys. Rev. Lett.* **112**, 054302 (2014).
31. Han, T. C., Bai, X., Thong, J. T. L., Li, B. W. & Qiu, C. W. Full control and manipulation of heat signatures: cloaking, camouflage and thermal metamaterials. *Adv. Mater.* **26**, 1731 (2014).
32. He, X. & Wu, L. Z. Illusion thermodynamics: a camouflage technique changing an object into another one with arbitrary cross section. *Appl. Phys. Lett.* **105**, 221904 (2014).
33. Yang, T. Z. et al. Invisible sensors: simultaneous sensing and camouflaging in multiphysical fields. *Adv. Mater.* **27**, 7752 (2015).
34. Yang, T. Z., Su, Y. S., Xu, W. K. & Yang, X. D. Transient thermal camouflage and heat signature control. *Appl. Phys. Lett.* **109**, 121905 (2016).
35. Hou, Q., Zhao, X., Meng, T. & Liu, C. Illusion thermal device based on material with constant anisotropic thermal conductivity for location camouflage. *Appl. Phys. Lett.* **109**, 103506 (2016).
36. Li, Y., Bai, X., Yang, T. Z., Luo, H. L. & Qiu, C. W. Structured thermal surface for radiative camouflage. *Nat. Commun.* **9**, 273 (2018).
37. Hu, R. et al. Illusion thermotic. *Adv. Mater.* **30**, 1707237 (2018).
38. Peng, X. Y. & Hu, R. Three-dimensional illusion thermotics with separated thermal illusions. *ES Energy Environ.* **6**, 39 (2019).
39. Hu, R. et al. Encrypted thermal printing with regionalization transformation. *Adv. Mater.* **31**, 1807849 (2019).
40. Zhang, J. W., Huang, S. Y. & Hu, R. Adaptive radiative thermal camouflage via synchronous heat conduction. *Chinese Phys. Lett.* **38**, 010502 (2021).
41. Zhou, S. L., Hu, R. & Luo, X. B. Thermal illusion with twinborn-like heat signatures. *Int. J. Heat Mass Transf.* **127**, 607–613 (2018).
42. Song, J. L. et al. Radiative metasurface for thermal camouflage, illusion and messaging. *Opt. Express* **28**, 875–885 (2020).
43. Liu, Y. D. et al. Dynamic thermal camouflage via a liquid-crystal-based radiative metasurface. *Nanophotonics* **9**, 855–863 (2020).
44. Hu, R. et al. Thermal camouflaging metamaterials. *Mater. Today* **45**, 120–141 (2021).
45. Li, Y. et al. Temperature-dependent transformation thermotics: from switchable thermal cloaks to macroscopic thermal diodes. *Phys. Rev. Lett.* **115**, 195503 (2015).
46. Li, Y., Shen, X. Y., Huang, J. P. & Ni, Y. S. Temperature-dependent transformation thermotics for unsteady states: switchable concentrator for transient heat flow. *Phys. Lett. A* **380**, 1641 (2016).
47. Shen, X. Y., Li, Y., Jiang, C. R., Ni, Y. S. & Huang, J. P. Thermal cloak-concentrator. *Appl. Phys. Lett.* **109**, 031907 (2016).
48. Dede, E. M., Nomura, T. & Lee, J. Thermal-composite design optimization for heat flux shielding, focusing, and reversal. *Struct. Multidiscipl. Optim.* **49**, 59 (2014).
49. Anflor, C. T. M., Albuquerque, E. L. & Wrobel, L. C. A topological optimization procedure applied to multiple region problems with embedded sources. *Int. J. Heat Mass Transf.* **78**, 121 (2014).
50. Han, T. C. et al. Manipulating steady heat conduction by sensu-shaped thermal metamaterials. *Sci. Rep.* **5**, 10242 (2015).
51. Yang, S., Xu, L. J., Wang, R. Z. & Huang, J. P. Full control of heat transfer in single-particle structural materials. *Appl. Phys. Lett.* **111**, 121908 (2017).
52. Fujii, G., Akimoto, Y. & Takahashi, M. Exploring optimal topology of thermal cloaks by CMA-ES. *Appl. Phys. Lett.* **112**, 061108 (2018).
53. Alekseev, G. V. & Tereshko, D. A. Particle swarm optimization-based algorithms for solving inverse problems of designing thermal cloaking and shielding devices. *Int. J. Heat Mass Transf.* **135**, 1269 (2019).
54. Fujii, G. & Akimoto, Y. Optimizing the structural topology of bifunctional invisible cloak manipulating heat flux and direct current. *Appl. Phys. Lett.* **115**, 174101 (2019).
55. Fujii, G. & Akimoto, Y. Cloaking a concentrator in thermal conduction via topology optimization. *Int. J. Heat Mass Transf.* **159**, 120082 (2020).
56. Hu, R. et al. Machine-learning-optimized aperiodic superlattice minimizes coherent phonon heat conduction. *Phys. Rev. X* **10**, 021050 (2020).
57. Dede, E. M., Schmalenberg, P., Nomura, T. & Ishigaki, M. Design of anisotropic thermal conductivity in multilayer printed circuit boards. *IEEE Trans. Compon. Packaging Manuf. Technol.* **5**, 1763 (2015).
58. Dede, E. M., Schmalenberg, P. & Nomura, T. Thermal metamaterials for heat flow control in electronics. *J. Electron. Packag.* **140**, 010904 (2017).
59. Park, G., Kang, S., Lee, H. & Choi, W. Tunable multifunctional thermal metamaterials: manipulation of local heat flux via assembly of unit-cell thermal shifters. *Sci. Rep.* **7**, 41000 (2017).
60. Kang, S. et al. Temperature-responsive thermal metamaterials enabled by modular design of thermally tunable unit cells. *Int. J. Heat Mass Transf.* **130**, 469 (2019).
61. Peralta, I., Fachinotti, V. & Ciarbonetti, Á. Optimization-based design of a heat flux concentrator. *Sci. Rep.* **7**, 40591 (2017).
62. Peralta, I. & Fachinotti, V. D. Optimization-based design of heat flux manipulation devices with emphasis on fabricability. *Sci. Rep.* **7**, 6261 (2017).
63. Fachinotti, V. D., Ciarbonetti, Á. A., Peralta, I. & Rintou, I. Optimization-based design of easy-to-make devices for heat flux manipulation. *Int. J. Therm. Sci.* **128**, 38 (2018).
64. Dede, E. M., Nomura, T., Schmalenberg, P. & Lee, J. S. Heat flux cloaking, focusing, and reversal in ultra-thin composites considering conduction-convection effects. *Appl. Phys. Lett.* **103**, 063501 (2013).
65. Hostos, J. C. A., Fachinotti, V. D., Peralta, I. & Tourn, B. A. Computational design of metadevices for heat flux manipulation considering the transient regime. *Numerical. Heat. Transfer., Part A*. **76**, 648 (2019).
66. Novoselov, K. S. et al. Electric field effect in atomically thin carbon films. *Science*. **306**, 666 (2004).
67. Bunch, J. S. et al. Impermeable atomic membranes from graphene sheets. *Nano Lett.* **8**, 2458 (2008).
68. Chen, S. et al. Oxidation resistance of graphenecoated Cu and Cu/Ni alloy. *ACS Nano*. **5**, 1321 (2011).
69. Su, Y. et al. Impermeable barrier films and protective coatings based on reduced graphene oxide. *Nat. Commun.* **5**, 4843 (2014).
70. Hayatdavoudi, H. & Rahsepar, M. A mechanistic study of the enhanced cathodic protection performance of graphene-reinforced zinc rich nanocomposite coating for corrosion protection of carbon steel substrate. *J. Alloy. Compd.* **727**, 1148 (2017).
71. Lin, K. T., Lin, H., Yang, T. H. & Jia, B. H. Structured graphene metamaterial selective absorbers for high efficiency and omnidirectional solar thermal energy conversion. *Nat. Commun.* **11**, 1389 (2020).
72. Z. Pu, in *Polymer Data Handbook*, (ed. J. E. Mark) (Oxford Univ. Press, New York, 1999).
73. Lin, J. et al. Laser-induced porous graphene films from commercial polymers. *Nat. Commun.* **5**, 5714 (2014).
74. Xi, W., Liu, Y. D., Song, J. L., Hu, R. & Luo, X. B. High-throughput screening of a high-Q mid-infrared Tamm emitter by material informatics. *Opt. Lett.* **46**, 888–891 (2021).
75. Ye, R. Q., James, D. K. & Tour, J. M. Laser-induced graphene. *Acc. Chem. Res.* **51**, 1609–1620 (2018).

Acknowledgements

The research was supported by “the Fundamental Research Funds for the Central Universities” (No. 3216002001A2).

Author contributions

W.X. initiated the project. L.Q. performed the experimental demonstrations with assistance from W.X. J.W. performed the data analysis and simulation. L.Q. and J.W. make the same contribution. All authors discussed the results and implications and commented on the paper at all stages. All authors wrote the paper and the Supplementary Information.

Competing interests

The authors declare no competing interests.

Additional information

Supplementary information The online version contains supplementary material available at <https://doi.org/10.1038/s43246-021-00196-1>.

Correspondence and requests for materials should be addressed to W.X.

Peer review information *Communications Materials* thanks the anonymous reviewers for their contribution to the peer review of this work. Primary Handling Editors: Aldo Isidori. Peer reviewer reports are available.

Reprints and permission information is available at <http://www.nature.com/reprints>

Publisher's note Springer Nature remains neutral with regard to jurisdictional claims in published maps and institutional affiliations.



Open Access This article is licensed under a Creative Commons Attribution 4.0 International License, which permits use, sharing, adaptation, distribution and reproduction in any medium or format, as long as you give appropriate credit to the original author(s) and the source, provide a link to the Creative Commons license, and indicate if changes were made. The images or other third party material in this article are included in the article's Creative Commons license, unless indicated otherwise in a credit line to the material. If material is not included in the article's Creative Commons license and your intended use is not permitted by statutory regulation or exceeds the permitted use, you will need to obtain permission directly from the copyright holder. To view a copy of this license, visit <http://creativecommons.org/licenses/by/4.0/>.

© The Author(s) 2021